Deformation of an Elastic Beam on a Winkler Foundation

Adam J. O. Butler [*]
BP Institute
Department of Earth Sciences
University of Cambridge
Cambridge UK, CB3 0EZ
Email: ajb278@cam.ac.uk

Colin R. Meyer
Assistant Professor of Engineering
Thayer School of Engineering
Dartmouth College
Hanover, NH 03755
Email: colin.r.meyer@dartmouth.edu

Jerome A. Neufeld
Reader in Earth and Planetary Fluid Dynamics
BP Institute
Department of Earth Sciences
Department of Applied Mathematics and Theoretical Physics
University of Cambridge
Cambridge UK, CB3 0EZ
Email: jn271@cam.ac.uk

We present a simple model for geophysical systems involving sources of deformation, such as magmatic intrusions, supraglacial lakes, and the subsurface storage of CO_2. We consider the idealised system of a uniform elastic layer overlying a localised region of constant pressure that is surrounded by a Winkler foundation composed of springs. We investigate the effect of source depth and foundation stiffness on the resulting displacement profiles at both the surface and the level of the source. The system is characterised by three key features: the maximum uplift, the maximum subsidence, and the distance to the point of zero displacement. For each of these we determine asymptotic scaling behaviour in the limits of a thin/thick layer and a soft/stiff foundation and form composite curves that allow specific parameter values to be determined from field data. Both two-dimensional and axisymmetric pressure patches are considered, and in the thin-layer limit we derive analytical solutions.

1 Introduction

There is a wide range of geophysical settings (for example volcanoes, glaciers, and geological CO_2 storage in aquifers) in which geodetic data can reveal details of the dynamical deformation of the subsurface environment and the processes involved. The development of geodetic measurement techniques such as InSAR and GPS has allowed the deformations associated with these geophysical processes to be scrutinised in more detail, leading to a better understanding of the source that causes these deformations [1,2].

These processes often produce a characteristic deformation profile that has a localised region of prominent uplift followed by a region of subsidence (see Fig.1b) that is reminiscent of the deflection produced by a bending beam over a soft medium, and distinct from the monotonic decay that is typical of a beam deforming over a rigid surface. This characteristic profile can be seen in the development of Uturuncu volcano in Bolivia [3] and as a result of supraglacial lake drainage in the Bindschadler Ice Stream in the West Antarctic Ice Sheet [4], for example.

In these settings, the deformation is typically the result of the build-up of pressure in some finite region below the surface (for example magma chambers, subglacial lakes, and injected CO_2 plumes). In order to forecast the system's future development, as well as understand its historical development, it is important to know the characteristics of this pressurised region - its size, its shape, its strength, and its depth - as well as the deformability of the surrounding material, both the overlying elastic material and the substrate. As direct interrogation of these regions is not possible, these characteristics must be inferred from remote geodetic sensing. We thus want to understand how each of these aspects of the physical setting affects the deformation profiles that result from these processes.

To do so, we use a simplified model of the material above the pressure source as an elastic beam supported by a Winkler foundation outside the pressurised region, from which we can calculate the deformation produced at the free surface above. In the 'thin layer' case, i.e. where the radius of the source is much larger than its depth and resulting

---

[*]Corresponding Author

deformations are small compared to the source depth, this system can be approximated by a bending beam, with a well-known analytical solution [5]. To be able to study a variety of source types we extend our model beyond this to include larger depth-to-radius ratios. In this paper, we focus on how the deformation profile depends upon the relative depth of the source and the 'stiffness' of the surrounding foundation. This allows us to study how the characteristics of the deformation profile depend on these parameters, and approximate this dependence using simple polynomial expressions. This significantly simplifies the inverse problem of determining these parameter values from observational data, reducing it from a complex PDE inversion to a simpler polynomial one.

Deformation due to isolated sources has previously been investigated and modelled in a variety of different ways, for example as an isolated source within an elastic halfspace [6–9] or for subglacial lakes and floating ice shelves using viscous or elastic ice rheologies [10–12]. The two most relevant to our present study are: the 'Penny-shaped Crack' model of Fialko et al. [6] for a similar finite pressure patch within a uniform elastic halfspace, with which we will directly compare our results; and the 'free-soft' ice-shelf model of Sayag and Worster [11] in which the grounded portion of the ice is modelled as a bending beam over a Winkler foundation, with which qualitative and analytical analogies can be drawn.

The outline of the paper is as follows. In §2 we consider the response of a finite elastic sheet, resting on a Winkler foundation, to a localised pressure source, and then in §3 discuss the mathematical analysis for this model and how we numerically solve for the surface deformation. We discuss the results for the 2D problem in §4.1 and for the axisymmetric problem in §4.2. In §5 we present the analytical solution in the thin-layer, bending beam limit. In §6 we discuss the results of our model, and finally in §7 we draw our conclusions.

2 Problem Setup

We consider the vertical displacement, w, within a two-dimensional elastic layer under gravity due to a composite pressure distribution applied at the base. We take the layer to have thickness h in the z direction (in the direction of gravity) and be infinite in the x direction (perpendicular to gravity); in the three-dimensional, axisymmetric case, the horizontal direction is described by the radial coordinate r. The layer has density ρ, shear modulus μ, and Poisson's ratio ν. The pressure distribution p is applied at $z = h$, and consists of a constant pressure patch around the centre of width $2R$ and strength P, and a Winkler pressure condition outside this region with Winkler modulus K. This setup is shown in Fig. 1a.

3 Mathematical Model

We now derive the relationship between the displacement $\mathbf{u} = (u, w)$ within the layer and the forces acting upon
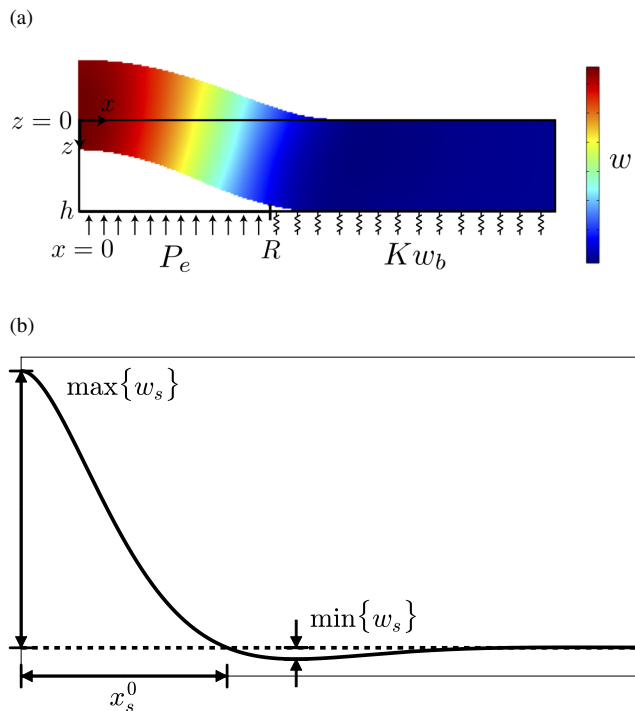

Fig. 1: The half-profile of the deformed elastic layer. (a) The pressure distribution applied to the base of the layer, with the colour denoting the amount of vertical displacement within the layer from our COMSOL simulations (b) The characteristic features of the displacement profile.

it. The analysis presented here can be readily extended from two dimensions to three dimensions.

For our problem, the pressure in excess of that supporting the weight of the layer, $p_e = p - \rho g h$, can be expressed as

$$p_e = \begin{cases} P_e & |x| \le R \\ K w_b & |x| > R \end{cases} = P_e T_R(x) + K w_b(x)[1 - T_R(x)],$$

(1)

where $P_e = P - \rho g h$ is the imposed excess pressure, w_b is the vertical displacement at the base ($z = h$), and $T_R(x)$ is the top-hat function defined to be 1 for $|x| < R$ and zero otherwise. Our aim is to determine the vertical displacements of the base, w_b, and the surface, w_s, as functions of x, h, and K.

On the base of the layer, at $z = h$, we impose the pressure distribution described above as well as zero traction. On the surface, at $z = 0$, we impose zero stress. As $|x| \to \infty$ we impose that all deformation of the elastic medium decays to zero. Finally, at $x = 0$ the shear stress $\mu(\partial w / \partial x)$ is automatically zero by symmetry.

To determine the relationship between pressure and displacement for an elastic layer of finite thickness in the vertical direction and infinite extent in the horizontal, we perform a similar analysis to that of Lu et al. [13], who considered a related problem but look for a solution that is axisymmetric with a no-displacement boundary condition rather than one of no-stress. The general theory of Boussinesq-Papkovich-

Neuber potential functions comes from Mindlin [14].

When the elastic medium is in equilibrium, its stress tensor σ_{ij} is related to the body forces F_i acting on the layer via the momentum equation

$$\sigma_{ij,j} + F_i = 0. \tag{2}$$

The linear constitutive relation between the stress tensor σ_{ij} and the strain tensor $\varepsilon_{ij} = (u_{i,j} + u_{j,i})/2$ can be written in terms of the displacement as

$$\sigma_{ij} = \mu \left(\frac{2\nu}{1-2\nu} \delta_{ij} u_{k,k} + u_{i,j} + u_{j,i} \right), \tag{3}$$

where μ is the layer's shear modulus and ν its Poisson's ratio. This allows us to express (2) in the form

$$\nabla^2 \mathbf{u} + \frac{1}{(1-2\nu)} \nabla (\nabla \cdot \mathbf{u}) = -\frac{1}{\mu} \mathbf{F}. \tag{4}$$

By Helmholtz's Theorem, $\mathbf{u}$ can be decomposed as $\mathbf{u} = \nabla \phi + \nabla \wedge \mathbf{H}$ with $\nabla \cdot \mathbf{H} = 0$.[1]

Equation (4) then becomes $\mu \nabla^2 \mathbf{B} = -\mathbf{F}$, where

$$\mathbf{B} = \alpha \nabla \phi + \nabla \wedge \mathbf{H}, \tag{5}$$

and $\alpha = 2(1-\nu)/(1-2\nu)$. By considering the divergence of $\mathbf{B}$, we can express ϕ as $\phi = (\mathbf{x} \cdot \mathbf{B} + \beta)/2\alpha$, where β obeys $\mu \nabla^2 \beta = \mathbf{x} \cdot \mathbf{F}$. Equation (4) can thus be rewritten in terms of the potentials $\mathbf{B}$ and β as

$$\mu \nabla^2 \mathbf{B} = -\mathbf{F}, \tag{6}$$

$$\mu \nabla^2 \beta = \mathbf{x} \cdot \mathbf{F}, \tag{7}$$

$$\mathbf{u} = \mathbf{B} - \frac{1}{4(1-\nu)} \nabla (\mathbf{x} \cdot \mathbf{B} + \beta). \tag{8}$$

For the problem at hand, the only body force acting on the elastic layer is gravity ($\mathbf{F} = \rho g \hat{\mathbf{z}}$), while the appropriate boundary conditions are

$$\sigma_{xz} = \sigma_{zz} = 0 \qquad \text{on } z = 0, \tag{9}$$
$$\sigma_{xz} = 0, \quad \sigma_{zz} = -p(x) \qquad \text{on } z = h. \tag{10}$$

Since there are no forces acting in the x direction, we set $B_x = 0$. By writing $B_z = \hat{B}_z - \rho g z^2/2\mu$ and $\beta = \hat{\beta} + \rho g z^3/6\mu$ we can transform to an equivalent problem that is free from body forces $\mathbf{F}$,

$$\nabla^2 \hat{B}_z = \nabla^2 \hat{\beta} = 0. \tag{11}$$

_____

[1] This is strictly applicable to three dimensions, i.e. $\mathbf{u} = (u, v, w)$. For our two-dimensional problem there is no variation in the y-direction so we set $v = 0$.

Here the only change to the boundary conditions (9) is that p is replaced by the effective pressure $p_e = p - \rho g h$. We now take w to be the vertical displacement of the layer measured from its equilibrium state when compressed by gravity, and h the thickness of the layer in this state.

We solve these Laplace equations by Fourier transforming $x \mapsto k_x$,

$$\tilde{f}(k_x) = \int_{-\infty}^{\infty} f(x) e^{-ik_x x} \, dx, \tag{12}$$

and expressing the transform of $\hat{\beta}$ in the form

$$\tilde{\beta}(k_x, z) = a_0(k_x) \sinh \bar{k} z + b_0(k_x) \cosh \bar{k} z, \tag{13}$$

where $\bar{k} = \sqrt{k_x^2} = |k_x|$ for real k_x, with a similar expression for $\tilde{B}_z$ in terms of coefficients a_1 and b_1. For variations in two horizontal dimensions, x and y, $\tilde{\beta}$ and $\tilde{B}_z$ would instead have coefficients that depend on both k_x and k_y, with $\bar{k}$ now given by $\bar{k} = \sqrt{k_x^2 + k_y^2}$.

By imposing the appropriate boundary conditions at $z = 0$ and $z = h$, we ultimately find that in spectral space the basal and surface displacements, w_b and w_s respectively, can be expressed in terms of the imposed excess pressure as

$$\tilde{w}_b = -\frac{2h(1-\nu^2)}{E} \frac{\sinh \tau \cosh \tau + \tau}{\tau [\sinh^2 \tau - \tau^2]} \tilde{p}_e(k_x), \tag{14}$$

$$\tilde{w}_s = -\frac{2h(1-\nu^2)}{E} \frac{\sinh \tau + \tau \cosh \tau}{\tau [\sinh^2 \tau - \tau^2]} \tilde{p}_e(k_x) \tag{15}$$

$$= \frac{\sinh \tau + \tau \cosh \tau}{\sinh \tau \cosh \tau + \tau} \tilde{w}_b, \tag{16}$$

where $\tau = h\bar{k}$, and $E = 2\mu(1+\nu)$ is the Young's modulus for the layer.

We now apply this general analysis to our specific problem. The excess pressure acting on the base of the layer is given by (1). By considering the asymptotic behaviour of the kernel in (14) as $\tau \to 0$ and $\tau \to \infty$, it is prudent to rewrite this pressure-displacement relation between p_e and w_b, (15), as

$$\tilde{p}_e(k_x) = \varsigma \tilde{\Lambda}(k_x) \cdot \left[(ik_x)^2 \tilde{w}_b(k_x) \right], \tag{17}$$

where $\tilde{p}_e$ and $\tilde{w}_b$ are the Fourier transforms of $p_e(x)$ and $w_b(x)$ respectively, with the Fourier transform defined by (12), and the elastic parameter ς and pressure-displacement kernel $\tilde{\Lambda}$ are given by

$$\varsigma = \frac{Eh}{2(1-\nu^2)}, \quad \tilde{\Lambda}(k_x) = \frac{\sinh^2(\tau) - \tau^2}{\tau [\sinh(\tau) \cosh(\tau) + \tau]}. \tag{18}$$

In physical space we thus have that

$$\varsigma (\Lambda * w_b'')(x) = P_e T_R(x) + K w_b(x)(1 - T_R(x)), \tag{19}$$

where $f*g$ is the convolution between f and g defined by

$$(f*g)(x) = \int_{-\infty}^{\infty} f(s)g(x-s)\,\mathrm{d}s. \qquad (20)$$

We note here that since $\tilde{\Lambda}$ is nondimensional, Λ has dimensions of inverse length while the convolution operator itself has dimensions of length for dimensionless functions f and g.

Following Fialko et al. [6], we nondimensionalise lengths by the patch radius R and stresses by the shear modulus of the layer μ. This produces the non-dimensional parameters

$$E^* = \frac{E}{\mu} = 2(1+\nu), \quad P^* = \frac{P}{\mu}, \quad K^* = \frac{KR}{\mu},$$

$$(x^*, z^*, w^*) = \frac{1}{R}(x, z, w), \quad h^* = \frac{h}{R}, \quad \varsigma^* = \frac{h/R}{(1-\nu)}. \qquad (21)$$

We immediately drop the * diacritic in order to avoid our equations becoming overly cluttered. Our nondimensional pressure–displacement equation is thus

$$\varsigma\left(\Lambda * w_b''\right)(x) = P_e T_1(x) + K w_b(x)\left[1 - T_1(x)\right]. \qquad (22)$$

It is not straightforward to unravel (22) analytically; a numerical approach is more tractable. Discretising the spatial domain as $x_j = -l + j\Delta x$ for $j = 0, 1, \ldots, n_x - 1$, where l is some artificial half-width for our numerical domain, Δx the grid spacing, and $n_x = 2l/\Delta x$ the number of grid points, we can write (22) in the form

$$[\mathbf{C} - K\mathrm{diag}(1 - \mathbf{T})]\mathbf{w} = P_e \mathbf{T}. \qquad (23)$$

Here $\mathbf{w}$ and $\mathbf{T}$ are vectors corresponding to $w_b(x_i)$ and $T_1(x_i)$, $\mathbf{C}$ is the convolution matrix given by

$$C_{ij} = \frac{\varsigma}{\Delta x}\Lambda(x_i - x_q)D_{qj}, \qquad (24)$$

and $\mathbf{D}$ is the second-order central-differences derivative matrix

$$\mathbf{D} = \begin{pmatrix} -2 & 1 & & & 0 \\ 1 & -2 & 1 & & \\ & \ddots & \ddots & \ddots & \\ & & 1 & -2 & 1 \\ 0 & & & 1 & -2 \end{pmatrix}. \qquad (25)$$

The function $\Lambda(x)$ is found by taking the inverse Fourier transform of $\tilde{\Lambda}(k_x)$ numerically. Since Λ decays towards infinity, if $(x_i - x_q)$ lies outside the appropriate range then we take $\Lambda(x_i - x_q)$ to be zero.

Table 1: Parameter values used for numerical simulations. The first section lists the fixed dimensional values used, while the second contains the corresponding nondimensional values. In our calculations either h^* or K^* is varied while the other remains fixed. For these we have listed both the values they take when held fixed and the ranges of values over which they are varied.

Parameter	Value	Units
ρ	917	kg/m^3
g	9.8	m/s^2
ν	0.3	-
R	10^3	m
E	9×10^9	Pa
P	2×10^8	Pa
h	10^3	m
K	10^8	Pa/m
l	5×10^4	m
Nondimensional values		
E^*	2.6	
P^*	5.778×10^{-2}	
h^*	1.0	$[10^{-2}$–$10^2]$
K^*	2.889×10^1	$[10^{-3}$–$10^8]$
l^*	5.000×10^1	

We now have a linear matrix problem (23) that we can invert to find $w_b(x)$ and $p_e(x)$. We could modify (23) in order to explicitly impose the boundary conditions that the solution tends to zero as $|x| \to \infty$ and that it has zero gradient at $x = 0$, however this is unnecessary as the natural solutions of this numerical system satisfy these automatically.

We are most interested in the deformation $w_s(x)$ at the free surface ($z = 0$). Once w_b has been determined, w_s may be found from the relation (16) between $\tilde{w}_s$ and $\tilde{w}_b$.

We also calculate these displacements by solving the linear elastic equations (2) and (3) directly using the software package COMSOL. In this approach we take one half of the domain considered above (i.e. $x \geq 0$), so the boundary condition $\partial w/\partial x = 0$ must be explicitly applied at $x = 0$. These two distinct approaches allow us to verify our results in the case of the 2D problem and then with confidence go on to use COMSOL to tackle the axisymmetric problem, to which the mathematical method described above could not readily be extended.

4 Numerical Results

The parameter values used for our numerical calculations are given in Tab. 1, including the default values of h and K. Here we report calculations for which $10^{-2} < h < 10^2$ and $10^{-3} < K < 10^8$ to span the range of different asymptotic behaviours. The default numerical domain has a half-width of $l^* = l/R = 50$, however in some simulations, e.g. for the largest values of h or smallest values of K, this was extended to as far as $l^* = 600$ in order to avoid artificial boundary effects.

We characterise the displacement profiles by three key properties:

1) the maximum displacement, $\max\{w_s\}$, which occurs over the centre of the pressure patch,
2) the minimum displacement, $\min\{w_s\}$, i.e the minimum uplift or maximum subsidence, which occurs outside the pressure patch,
3) the location of zero displacement closest to the pressure patch, x_s^0.

The latter can also be substituted for the location at which the minimum displacement occurs, which behaves in a similar manner. These features are shown in Fig. 1b.

Below we demonstrate, for both the 2D and axisymmetric problems, how the surface displacement and its three key characteristics vary as either the layer thickness h or Winkler modulus K is varied while the other is held constant. As we are primarily interested in the surface displacement, those results are displayed here. The corresponding results for the basal displacement are reported in the Appendix.

4.1 Two-dimensional results

We begin by detailing the functional form of the displacement and the asymptotic scalings as a function of layer thickness, h, and the strength of the Winkler foundation, K. The results of our two-dimensional calculations are shown in Fig. 2-7. In Fig. 2 we compare the surface displacement profiles in the four corners of our (h, K) parameter range. Each has been rescaled by its respective maximum displacement and location of zero displacement, and is shown against a large-K bending-beam solution.

The behaviour of these characteristic features as h is varied is shown in Fig. 3-6. In each case we find an asymptotic power-law behaviour for either $h \ll 1$ or $h \gg 1$, with the corresponding asymptotic scalings listed in Tab. 2. In the thin-layer limit, $h \ll 1$, our system reduces to that of a bending beam, which can be solved analytically. We review this solution in §5, and our numerical results agree well with the bending-beam solution in the thin-layer limit.

In the case of varying h, we find that the maximum and minimum displacements decrease monotonically with increasing h, i.e. are largest for a thin layer; thinner layers are more easily deformable. The location of zero displacement, meanwhile, increases monotonically with h. Each of Fig. 3-6 shows results for three different fixed values of K. For a given value of h, the amount of displacement and its horizontal extent increase with decreasing K, as expected;

Table 2: Surface displacement scaling behaviours for two-dimensional deformations.

	$h \ll 1$	$h \gg 1$	$K \ll 1$	$K \gg 1$
$\max\{w_s\}$	h^{-3}	h^{-1}	$K^{-3/4}$	K^0
$\min\{w_s\}$	$h^{-3/2}$	h^{-1}	$K^{-3/4}$	K^0
x_s^0	h^0	h^1	$K^{-1/4}$	K^0

softer foundations are more pliable. The corresponding results for our COMSOL calculations using the default value of K are also displayed in each of the figures, and show excellent agreement between the two methods.

For the case of varying K, we restrict ourselves for brevity to displaying only the variation of the maximum surface displacement in Fig. 7 and otherwise quoting the appropriate scalings in Tab. 2. As discussed above, the vertical and horizontal displacement features decrease with increasing K, as expected. Importantly, each of these becomes insensitive to K for $K \gg 1$, tending in this limit to constant values, the precise values of which are dependent on h.

Outside of the $h, K = O(1)$ region of our parameter space, the solution takes on the asymptotic scaling behaviour detailed in Tab. 2. For a thin layer, $h \ll 1$, we recover the bending-beam solution discussed in §5. As h is increased, we ultimately reach the deep elastic limit often considered for this type of deformation model [6–9]. Similarly, as the Winkler modulus K is varied there are two different asymptotic behaviours, corresponding to a soft foundation, $K \ll 1$, or a stiff foundation, $K \gg 1$. From our numerical results we find that these asymptotic regions are well established for $h < 10^{-1}$, $h > 10^1$, $K < 10^{-2}$, and $K > 10^2$, respectively.

The behaviour of each of these displacement features can be well approximated by composite curves for varying h or K, built as simple power series based on these asymptotic scalings. These are shown by the dashed lines in the figures and allow the parameter values of the system such as h, K, and P_e to be inferred from measurements of these displacement features. For each curve we have chosen the coefficients and intermediate powers so that the relative error between the curves and the numerical data is less than 10%. For example, the maximum surface displacement as a function of h is approximated by

$$\max\{w_s\} \sim c_0 h^{-3} + c_1 h^{-5/2} + c_2 h^{-4/2} + c_3 h^{-3/2} + c_4 h^{-1}, \tag{26}$$

where the coefficients for the three values of K shown in Fig. 3-6 are given in Tab. 3. The remaining composite curves are discussed in the Supplementary Material.

4.2 Axisymmetric results

We now consider the axisymmetric case of a three-dimensional elastic layer, forced on its lower face by a circular patch of radius R and constant excess pressure P_e, outside
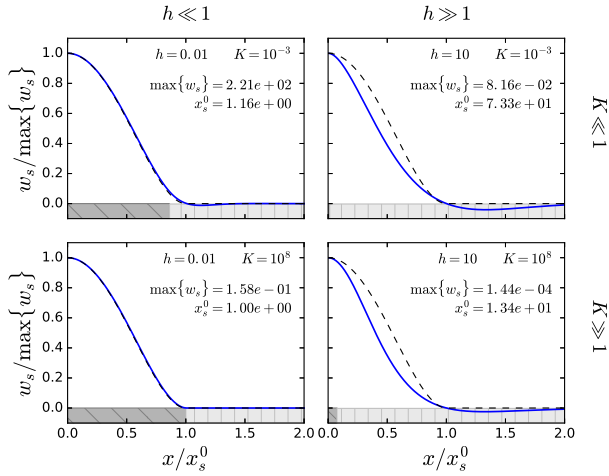
Fig. 2: Comparison of two-dimensional surface profiles for different (h, K) values. The solid blue curves are for the parameter values quoted and the dashed curves are the bending-beam solution (29) for $h = 10^{-4}$, $K = 10^8$, shown for comparison. The dark-grey, obliquely hatched region shows the section of the displacement overlying the pressure patch, while the light-grey, vertically hatched region denotes the Winkler foundation.
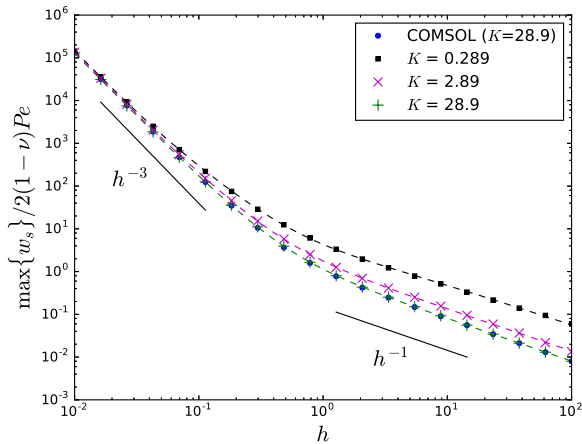

Fig. 3: Maximum surface displacement versus layer thickness h, rescaled to match Fig. 2 of Fialko et al. [6]. The results of both methods used are shown for $K = 28.9$. The dashed lines are composite curves formed from the scaling behaviours for $h \ll 1$ and $h \gg 1$.

of which we have the Winkler pressure $K w_b$ as before.

The approach detailed in Sec. 4.1 can not be readily extended to the axisymmetric problem, as the left-hand side of the equivalent to (22) is not so easily discretised to form a matrix equation. We thus only present the COMSOL simulations for axisymmetric deformations, which we have verified for purely two-dimensional deformations by comparison with the mathematical model in the previous section. The asymptotic scalings for each feature are listed in Tab. 4.

Figure 8 shows the axisymmetric surface displacement
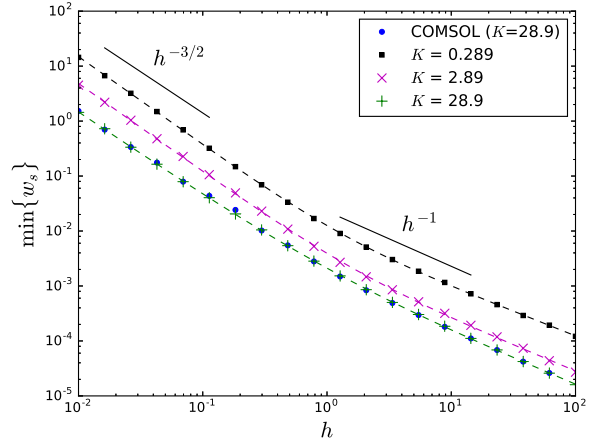
Fig. 4: Minimum surface displacement versus layer thickness h.
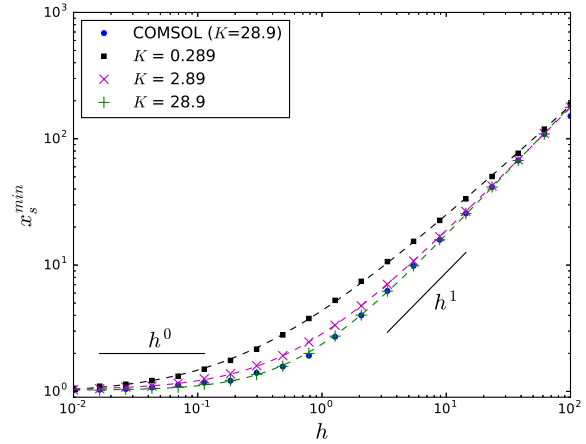
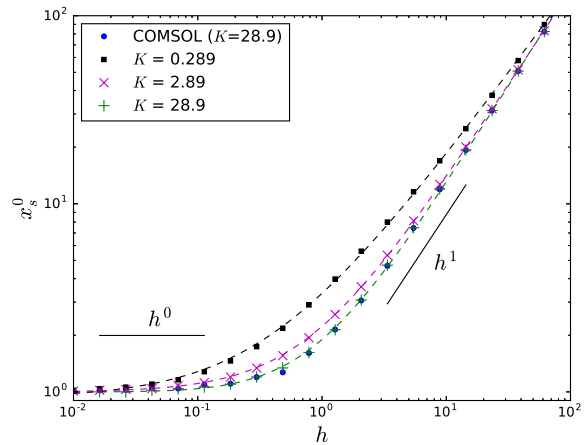Fig. 5: Location of minimum surface displacement versus layer thickness h.

Fig. 6: Horizontal location of zero surface displacement versus layer thickness h.
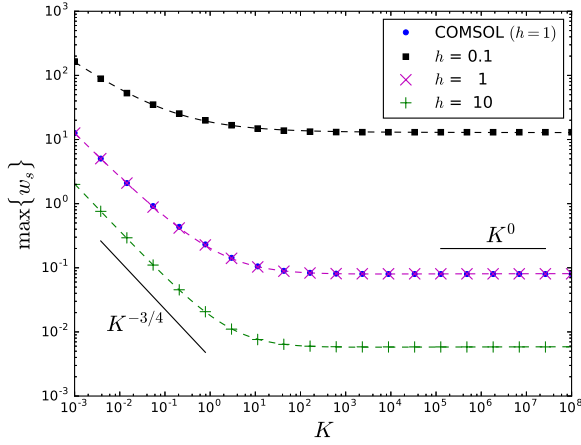
Fig. 7: Maximum surface displacement versus Winkler Modulus K.

Table 3: Coefficients for the composite curves constructed for $\max\{w_s\}$ for two-dimensional deformations.

$K = 2.89\times$	10^{-1}	10^{0}	10^{1}
c_0	0.014156	0.009578	0.009603
c_1	-0.055806	0.008799	0.00625
c_2	0.381111	0.043843	0.021327
c_3	-0.491104	-0.034164	-0.011244
c_4	0.501753	0.115059	0.066257

Table 4: Surface displacement scaling behaviours for axisymmetric deformations.

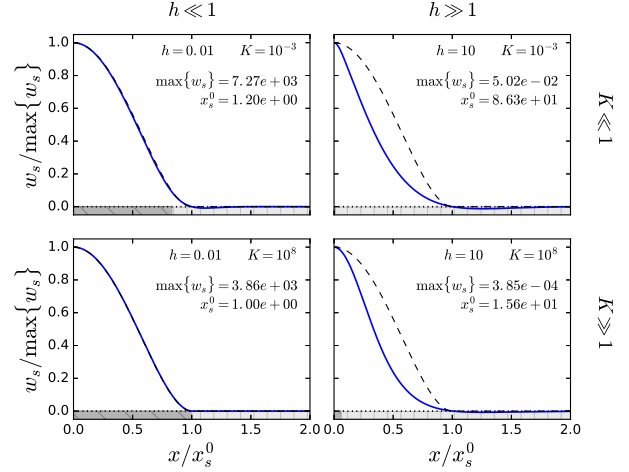|	$h \ll 1$	$h \gg 1$	$K \ll 1$	$K \gg 1$
$\max\{w_s\}$	h^{-3}	h^{-2}	$K^{-1/2}$	K^0
$\min\{w_s\}$	$h^{-3/2}$	h^{-2}	$K^{-1/2}$	K^0
r_s^0	h^0	h^1	$K^{-1/4}$	K^0

Fig. 8: Comparison of axisymmetric surface profiles for different (h, K) values. The solid blue curves are for the parameter values quoted while the dashed curves are the bending-beam solution (45) for $h = 10^{-2}$, $K = 10^4$.

profiles that occur for the four combinations of small/large h and small/large K, rescaled by their respective maximum displacement values and zero displacement locations. These profiles broadly mimic those seen for two-dimensional deformations as illustrated in Fig. 2. We see that h has a dominant effect on the profile in the uplift region near the pressure patch, while K affects the curvature within this region as well as the depth of the region of subsidence.

The value of the maximum displacement as h is varied is shown in Fig. 9, rescaled based on the $h \ll 1$ bending-beam solution discussed in §5 in order to match Fialko et al.'s Figure 2 [6]. Under this rescaling the limiting value for $h \ll 1$ is $(3/64)h^{-3}$, which is independent of K. Along with our results, we have also plotted values calculated using the method described in [6]. These agree well with our $K = 28.89$ curve throughout the range of values of h considered. As can be seen from Fig. 7, this value of K lies in the stiff-foundation, $K \gg 1$ region of our parameter space.

We again find that the maximum and minimum displacements decrease monotonically with increasing h, while the zero location increases with h. For $h \ll 1$ we recover the same h^{-3} scalings as for the two-dimensional problem, however for $h \gg 1$ the maximum and minimum displacements

decrease at a faster rate (h^{-2}) for the axisymmetric problem. For varying K, each of the characteristic features now grows with decreasing K and is again insensitive to large K, tending to constant values in this limit. The axisymmetric problem thus shows the same qualitative behaviour as the two-dimensional problem, but differs quantitatively in terms of specific scalings and coefficients.

The maximum surface displacement results are well approximated by the composite curve

$$\max\{w_s\} \sim c_0 h^{-3} + c_1 h^{-11/4} + c_2 h^{-10/4} + c_3 h^{-9/4} + c_4 h^{-2}, \quad (27)$$

where the coefficients for the three values of K shown in Fig. 9 are given in Tab. 5. The remaining composite curves are discussed in the Supplementary Material.

5 Analytic solutions
5.1 Two-dimensional problem

For two-dimensional deformations we are able to solve (22) analytically in the bending-beam limit, $h \ll 1$. By considering the small-h behaviour of the pressure–displacement kernel in (14) we find that in this limit $w_b(x) = w_s(x) = w(x)$
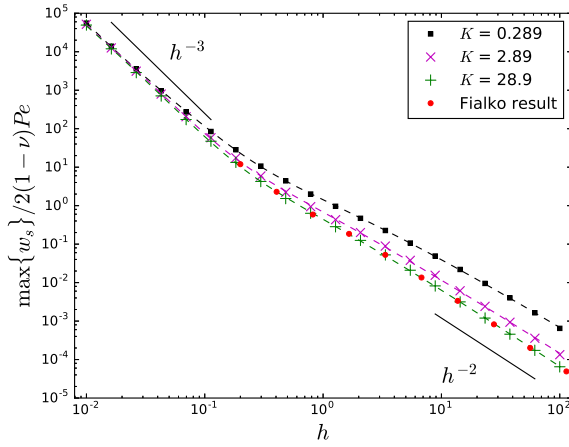
Fig. 9: Axisymmetric plot of the maximum displacement. The red dots show the results from Fig. 2 of Fialko et al. [6].

Table 5: Coefficients for the composite curves constructed for $\max\{w_s\}$ for axisymmetric deformations.

$K = 2.89\times$	10^{-1}	10^0	10^1
c_0	0.056587	-0.01107	-0.011976
c_1	-0.452762	0.083362	0.100009
c_2	1.426684	-0.1134	-0.196063
c_3	-1.957016	-0.0446	0.107734
c_4	1.041727	0.140847	0.036067

and (22) becomes

$$-\mathcal{B}\frac{\mathrm{d}^4}{\mathrm{d}x^4}w(x) = P_e T_1(x) + K w(x)[1 - T_1(x)], \quad (28)$$

where in our formulation the bending stiffness of the layer is given by $\mathcal{B} = h^3/6(1-\nu)$.

By solving this equation in the two regions $|x| < 1$ and $|x| > 1$ such that $w(x)$ is even about $x = 0$ and the function and its first three derivatives are continuous at $|x| = 1$, we arrive at

$$w(x) = -\frac{P_e}{\mathcal{B}}\begin{cases}(x^4/4! + d_2 x^2/2! + d_0) & |x| < 1 \\ e^{\kappa(1-|x|)}(A_1 \cos\kappa|x| + A_2 \sin\kappa|x|) & |x| > 1\end{cases}, \quad (29)$$

where $\kappa^{-1} = \sqrt{2}(\mathcal{B}/K)^{1/4}$ is the length scale of deformations outside the pressure patch. We note that because of our choice of orientation for the z axis, surface uplift takes negative values.

From the boundary conditions we find that the coeffi-

cients in (29) may be expressed as

$$d_2 = -\frac{1}{6}\frac{(\kappa^2 + 3\kappa + 3)}{\kappa(\kappa+1)}, \quad (30)$$

$$d_0 = \frac{1}{24}\frac{(\kappa^4 + 5\kappa^3 + 10\kappa^2 + 12\kappa + 6)}{\kappa^3(\kappa+1)}, \quad (31)$$

$$A_1 = \frac{1}{12}\frac{(2\kappa^2 + 6\kappa + 3)\cos\kappa + (2\kappa^2 - 3)\sin\kappa}{\kappa^3(\kappa+1)}, \quad (32)$$

$$A_2 = \frac{1}{12}\frac{(2\kappa^2 + 6\kappa + 3)\sin\kappa - (2\kappa^2 - 3)\cos\kappa}{\kappa^3(\kappa+1)}. \quad (33)$$

We are particularly interested in the limiting behaviour of this solution as the length scale $\kappa^{-1} \propto h^{3/4}K^{-1/4}$ becomes either large or small. In particular, for $K \gg 1$ (such that $\kappa^{-1} \ll 1$) we find that $d_2 \sim (-1/6) + O(\kappa^{-1})$ and $d_0 \sim (1/24) + O(\kappa^{-1})$, and so at leading order we recover the well-known bending-beam profile $w \propto (1 - x^2)^2$ for $|x| < 1$ [5].

Continuing this for the characteristic features of our displacement profiles, we find that the maximum value of the displacement, occurring at $x = 0$, is given by

$$w(0) \sim \begin{cases} -\left[\frac{3}{2}(1-\nu)\right]^{1/4} P_e h^{-3/4} K^{-3/4} & \kappa^{-1} \gg 1 \\ -\frac{1}{4}(1-\nu) P_e h^{-3} K^0 & \kappa^{-1} \ll 1 \end{cases}. \quad (34)$$

As expected from the physical nature of the problem, the minimum displacement must occur at a point x_{min} outside the pressure patch, in the region $|x| > 1$. A local maximum or minimum of the displacement can be shown to occur in this region when

$$\tan(\kappa x_{min}) = \frac{A_2 - A_1}{A_2 + A_1}, \quad (35)$$

which can be manipulated to give

$$\tan(\kappa[x_{min} - 1]) = -\frac{\kappa(2\kappa + 3)}{3(\kappa+1)}. \quad (36)$$

For $\kappa^{-1} \gg 1$ we can expand this expression to find

$$\kappa x_{min} \sim n\pi + \frac{1}{3}\kappa^2 + O(\kappa^3). \quad (37)$$

Because the displacement decays away from the pressure patch, the minimum displacement corresponds to the first stationary point outside of $x = 1$. We thus take $n = 1$ here. As discussed in [11], in the $\kappa^{-1} \gg 1$ limit the distance between stationary points gives us information about the natural wavenumber of the system: $(x_{stat}^{n+1} - x_{stat}^n) \sim \kappa/3$.

For $\kappa^{-1} \ll 1$ we instead consider the reciprocal of (36) and, expanding in large κ, find that

$$\kappa x_{min} \sim \kappa + \frac{\pi}{2} + \frac{3}{2}\kappa^{-1} + O(\kappa^{-2}). \quad (38)$$

Thus in the two limits we have that

$$x_{min} \sim \begin{cases} \pi \left[\frac{3}{2}(1-\nu)\right]^{-1/4} h^{3/4} K^{-1/4} & \kappa^{-1} \gg 1 \\ 1 + \frac{\pi}{2}\left[\frac{3}{2}(1-\nu)\right]^{-1/4} h^{3/4} K^{-1/4} & \kappa^{-1} \ll 1 \end{cases}. \quad (39)$$

Having determined x_{min}, we can now find the value of the minimum displacement. After some algebra, we find that

$$w(x_{min}) = \frac{P_e}{\mathcal{B}} \frac{\sqrt{4\kappa^4 + 12\kappa^3 + 18\kappa^2 + 18\kappa + 9}}{12\kappa^3(\kappa+1)} e^{-\kappa(x_{min}-1)}. \quad (40)$$

Using the above behaviours of x_{min} for large and small κ^{-1}, we find that

$$w(x_{min}) \sim \begin{cases} \left[\frac{3}{2}(1-\nu)\right]^{1/4} e^{-\pi} P_e h^{-3/4} K^{-3/4} & \kappa^{-1} \gg 1 \\ \left[\frac{2}{3}(1-\nu)\right]^{1/2} e^{-\pi/2} P_e h^{-3/2} K^{-1/2} & \kappa^{-1} \ll 1 \end{cases}. \quad (41)$$

Finally, we can also determine the first zero crossing of the deformation, x_0. We can again see that this must occur in the region $|x| > 1$, and from (29) we find that x_0 satisfies $\tan(\kappa x_0) = -A_1/A_2$. This can similarly be manipulated into the form

$$\tan(\kappa[x_0 - 1]) = \frac{2\kappa^2 + 6\kappa + 3}{2\kappa^2 - 3}, \quad (42)$$

from which we extract the scalings for the first zero crossing

$$x_0 \sim \begin{cases} \frac{3\pi}{4}\left[\frac{3}{2}(1-\nu)\right]^{-1/4} h^{3/4} K^{-1/4} & \kappa^{-1} \gg 1 \\ 1 + \frac{\pi}{4}\left[\frac{3}{2}(1-\nu)\right]^{-1/4} h^{3/4} K^{-1/4} & \kappa^{-1} \ll 1 \end{cases}. \quad (43)$$

5.2 Axisymmetric Problem

In the previous section we considered the problem of variation over one horizontal dimension in the bending-beam limit. For two horizontal dimensions, we find that (22) reduces to a biharmonic equation, i.e. the left-hand side of (28) changes to $-\mathcal{B}\nabla^4 w(x,y)$. For axisymmetric deformations in the limit $h \ll 1$, the governing equation is then

$$-\mathcal{B}\left[\frac{1}{r}\frac{d}{dr}\left(r\frac{d}{dr}\right)\right]^2 w(r) = P_e T_1(r) + Kw(r)[1 - T_1(r)], \quad (44)$$

where the differential operator within the square brackets is applied twice. As before we solve this for the regions $r < 1$ and $r > 1$ and connect the two solutions by requiring that w and its first three derivatives are continuous at $r = 1$. This gives

$$w(r) = -\frac{P_e}{\mathcal{B}} \begin{cases} (r^4/64 + \hat{d}_2 r^2/2 + \hat{d}_0) & r < 1 \\ \left(2\Re\left\{\hat{A}H_0^{(1)}(\hat{\omega}r)\right\}\right) & r > 1 \end{cases}, \quad (45)$$

where $\Re\{z\}$ denotes the real part of z, $\hat{\omega} = e^{i\pi/4}\hat{\kappa}$ with $\hat{\kappa}^{-1} = (\mathcal{B}/K)^{1/4}$, and $H_0^{(1)}(z)$ is the zeroth-order Hankel function of the first kind. Our continuity conditions at the edge of the pressure patch set the coefficients $\hat{d}_2$, $\hat{d}_0$, and $\hat{A}$ to be

$$\hat{d}_2 = 2\Re\left\{\hat{A}\hat{\omega}H_0^{(1)\prime}(\hat{\omega})\right\} - \frac{1}{16}, \quad (46)$$

$$\hat{d}_0 = 2\Re\left\{\hat{A}H_0^{(1)}(\hat{\omega})\right\} - \frac{1}{2}\hat{d}_2 - \frac{1}{64}, \quad (47)$$

$$\overline{(16i\hat{\kappa}^4\Psi\hat{A})} = \left(\left[8\hat{\omega} - \hat{\omega}^3\right]H_0^{(1)\prime}(\hat{\omega}) + 4\hat{\omega}^2 H_0^{(1)}(\hat{\omega})\right), \quad (48)$$

with

$$\Psi = \left[\Im\left\{e^{-i\pi/4}\hat{\kappa}H_0^{(1)}(\hat{\omega})\overline{H_0^{(1)\prime}(\hat{\omega})}\right\} - 2\left|H_0^{(1)\prime}(\hat{\omega})\right|^2\right], \quad (49)$$

where $\Im\{z\}$ denotes the imaginary part of z while $\bar{z}$ denotes its complex conjugate.

Our main interest is how this solution behaves in the limit of small h, i.e. in the small wavelength limit where $\hat{\kappa}^{-1} = (\mathcal{B}/K)^{1/4} \ll 1$. In this limit the radius of curvature of the pressure patch is much larger than the wavelength of the induced displacement, and so at leading order the system does not feel this curvature and shares the same limiting behaviour as the two-dimensional solution, up to a constant multiple for the vertical displacements. This constant is set by matching the solution across $r = 1$, with the axisymmetric and two-dimensional solutions differing over the pressure patch due to volume considerations. By comparing the $r < 1$ quartic solutions in the two cases, we find that

$$w^{axi}(1) \sim \frac{3}{8}w^{2D}(1) \quad \text{for } (\mathcal{B}/K)^{\frac{1}{4}} \ll 1. \quad (50)$$

Hence, for the axisymmetric case we have that in the limit $\hat{\kappa}^{-1} \ll 1$:

$$w(0) \sim -\frac{3}{32}(1-\nu)P_e h^{-3} K^0, \quad (51)$$

$$w(r_{min}) \sim \left[\frac{3}{32}(1-\nu)\right]^{1/2} e^{-\pi/2} P_e h^{-3/2} K^{-1/2}, \quad (52)$$

$$r_{min} \sim 1 + \frac{\pi}{2}\left[\frac{3}{2}(1-\nu)\right]^{-1/4} h^{3/4} K^{-1/4}, \quad (53)$$

$$r_0 \sim 1 + \frac{\pi}{4}\left[\frac{3}{2}(1-\nu)\right]^{-1/4} h^{3/4} K^{-1/4}. \quad (54)$$

Conversely, in the long-wavelength limit the axisymmetric solution departs from the two-dimensional case. Using the asymptotic behaviour $H_0^{(1)}(z) \sim 1 + (2i/\pi)\log z$ for $|z| \ll 1$

[15], we find that for $\hat{\kappa}^{-1} \gg 1$:

$$w(0) \sim -\pi \left[\frac{3}{32} (1-\nu) \right]^{1/2} P_e h^{-3/2} K^{-1/2}, \qquad (55)$$

$$w(r_{min}) \sim \pi \chi \left[\frac{3}{8} (1-\nu) \right]^{1/2} P_e h^{-3/2} K^{-1/2}, \qquad (56)$$

$$r_{min} \sim \eta_1 \left[6(1-\nu) \right]^{-1/4} h^{3/4} K^{-1/4}, \qquad (57)$$

$$r_0 \sim \eta_0 \left[6(1-\nu) \right]^{-1/4} h^{3/4} K^{-1/4}. \qquad (58)$$

Here $\eta_0 \approx 3.9147$ and $\eta_1 \approx 4.9318$ are the first real zeros of $\Re\{H_0^{(1)}\left(e^{i\pi/4}z\right)\}$ and $\Re\{e^{i\pi/4}H_1^{(1)}\left(e^{i\pi/4}z\right)\}$ respectively, and $\chi = -\Re\{H_0^{(1)}\left(e^{i\pi/4}\eta_1\right)\}$.

6 Discussions

The calculations in §4 have been performed for specific parameter values of P_e, h, K, etc. In practice, however, it is more common to want to determine the parameter values of the system from the surface displacement profiles. This can be done using the composite curves introduced in §4 and discussed in detail in the Supplementary Material. Comparing the normalised displacement profile to Fig. 2 or Fig. 8 first allows the appropriate region of the (h, K) parameter space to be determined. The values of the three nondimensionalised characteristic features can then be compared against the corresponding composite curves in the appropriate parameter intervals in order to bound or approximate the desired parameter values. These composite curves thus simplify the inverse problem significantly, converting it from a complex PDE problem to a simple polynomial one. This could then be used to substantially reduce the region of parameter space considered in a more sophisticated model.

Our model has assumed a linear elastic rheology for the layer with displacements only in the vertical direction. If the resulting deformations become too large then the behaviour of the system would change: this linearity assumption could fail; horizontal deformations, in-plane tensions, and shear could become important; or fracturing may occur within the layer, allowing cracks to form or further develop. The strength of the pressure patch plays a crucial role in all three of these, as the deformations are proportional to P_e (see (22)). For large enough strains the constitutive relation between stress and strain will become nonlinear, with the precise threshold for 'large enough' dependent upon the particular constitutive relation for the material considered.

Fracturing is likely to first occur within the pressure patch when P_e exceeds some threshold value dependent on the material properties of the layer. Incorporating a finite fracture toughness adds an energy penalty that impedes the opening of a fracture. For a thin layer, this energy penalty imposes a jump condition on the curvature at the fracture tip [16]. For a thick layer, this penalty can instead be described by the Griffith–Irwin model

$$\sigma_f = \sqrt{\frac{(1-\nu^2)}{\pi l_c}} \mathcal{K}, \qquad (59)$$

where σ_f is the stress at the fracture tip; l_c is the length of the crack; ν is the Poisson ratio of the material; and $\mathcal{K}$ is its Stress Intensity Factor, which is a function of the fracture profile and the distribution of the applied stress [17]. Our model could be extended to include fracturing by determining the stress at the base of the layer during the finite element calculations discussed above and comparing this to the Griffith-Irwin criterion (59) - if this criterion is met then the patch size must be adjusted before the deformation calculations are continued. For a study of the development of such a fracture with zero fracture toughness in the case of intraglacial fluid channelisation, see Tsai & Rice [18]. Alternatively, the porous nature of a poroelastic till may play a critical role in the development of a cavity during supraglacial lake drainage. A representation of the fluid dynamics of this process is described in Hewitt et al. [19].

In certain settings, such as supraglacial lakes near the edge of a glacier, finite-length effects may also be important. The geometrical constraint of a fixed, finite length changes the behaviour of the layer as it deforms. The bending-beam model of Sayag and Worster [11] gives the rough estimate that these effects will be negligible for our layer if its half-width is at least five times the elastic wavelength $(\mathcal{B}/K)^{1/4}$, where $\mathcal{B} = h^3/[6(1-\nu)]$ is the bending stiffness defined in §5.1. In a similar manner, the interaction between two such pressure regions would become important if they are sufficiently close together. Further work is required to determine at what point these effects may play a significant role in the pattern of deformation, in particular in cases when the layer is not thin.

7 Conclusions

We have presented a simplified model that is applicable to many systems of geophysical importance involving surface deformation, treating the deforming material as a uniform elastic layer overlying a patch of constant pressure that is surrounded by a Winkler foundation. Examples of such systems include magmatic intrusions, supraglacial lakes, and the subsurface storage of CO_2.

The displacement is characterised by three key features: the maximum uplift, the maximum subsidence, and the distance from the centre to the location of zero displacement. We have determined asymptotic scalings for each of these features in the limits of a thin/thick layer and a soft/stiff foundation. In particular, we find that once the stiffness parameter is large enough these features become insensitive to it. In the limit of a thin layer, our results match well with the analytical bending-beam solutions presented in §5.

Based on these scalings, we have presented composite curves for each of these characteristic features, with which it is possible to determine properties of the system such as the

strength of the pressure patch, the depth of the patch relative to its width, and the stiffness of the surrounding foundation. These properties can then be used to better understand the current or future behaviour of the subsurface processes that have produced the deformation.

We find qualitative similarity between the two-dimensional and axisymmetric problems, but there are distinct quantitative differences between the corresponding scaling exponents and coefficients. In the axisymmetric problem we recover the elastic-halfspace results of Fialko et al. [6] for a stiff foundation. The corresponding displacement profiles are different however, as our system allows for a region of subsidence. We are thus able to reproduce their 'penny-shaped crack' results using a simpler mathematical model and extend them to the case of a soft foundation.

Acknowledgements

Nomenclature

$\mathcal{B}$ bending stiffness, $h^3/6(1-\nu)$
E Young's modulus
$\tilde{f}(x)$ Fourier transform of $f(x)$
g gravitational acceleration
h layer thickness
k_x horizontal wavenumber (corresponding to x)
K Winkler modulus
p_e excess pressure, $p - \rho g h$
R radius of pressure patch
w vertical displacement
w_b, w_s vertical displacement (at base, surface of layer)
x horizontal coordinate
z vertical coordinate (in direction of gravity)
ε_{ij} strain tensor
$\kappa, \hat{\kappa}$ inverse length scales of bending-beam solutions (two-dimensional, axisymmetric)
Λ pressure-displacement kernel
μ shear modulus
ν Poisson's ratio
ρ density
ς elastic parameter, $Eh/2(1-\nu^2)$
σ_{ij} stress tensor

References

[1] Simons, M., and Rosen, P., 2007. "3.12 - Interferometric Synthetic Aperture Radar Geodesy". In *Treatise on Geophysics*, G. Schubert, ed. Elsevier, Amsterdam, pp. 391 – 446.

[2] Segall, P., and Davis, J. L., 1997. "GPS applications for geodynamics and earthquake studies". *Annual Review of Earth and Planetary Sciences,* **25**(1), pp. 301–336.

[3] Henderson, S. T., and Pritchard, M. E., 2017. "Time-dependent deformation of Uturuncu volcano, Bolivia,

[4] Gray, L., Joughin, I., Tulaczyk, S., Spikes, V. B., Bindschadler, R., and Jezek, K., 2005. "Evidence for subglacial water transport in the West Antarctic Ice Sheet through three-dimensional satellite radar interferometry". *Geophysical Research Letters,* **32**(3).

[5] Landau, L., and Lifshitz, E., 1986. *Theory of Elasticity*. Pergamon Press, Pergamon Press Ltd., Headington Hill Hall, Oxford.

[6] Fialko, Y., Khazan, Y., and Simons, M., 2001. "Deformation due to a pressurized horizontal circular crack in an elastic half-space, with applications to volcano geodesy". *Geophysical Journal International,* **146**(1), pp. 181–190.

[7] Mogi, K., 1958. "Relations between the eruptions of various volcanoes and the deformations of the ground surfaces around them". *Bulletin of the Earthquake Research Institute, University of Tokyo,* **36**, pp. 99–134.

[8] Okada, Y., 1985. "Surface deformation due to shear and tensile faults in a half-space". *Bulletin of the seismological society of America,* **75**(4), pp. 1135–1154.

[9] Sun, R. J., 1969. "Theoretical size of hydraulically induced horizontal fractures and corresponding surface uplift in an idealized medium". *Journal of Geophysical Research,* **74**(25), pp. 5995–6011.

[10] Walker, R. T., Werder, M. A., Dow, C. F., and Nowicki, S. M., 2017. "Determining ice-sheet uplift surrounding subglacial lakes with a viscous plate model". *Frontiers in Earth Science,* **5**, p. 103.

[11] Sayag, R., and Worster, M. G., 2011. "Elastic response of a grounded ice sheet coupled to a floating ice shelf". *Phys. Rev. E,* **84**, Sep, p. 036111.

[12] Wagner, T. J., James, T. D., Murray, T., and Vella, D., 2016. "On the role of buoyant flexure in glacier calving". *Geophysical Research Letters,* **43**(1), pp. 232–240A.

[13] Lu, M., Huang, S., Yang, X., Yang, L., and Mao, R., 2017. "Semianalytical solution for the deformation of an elastic layer under an axisymmetrically distributed power-form load: Application to fluid-jet-induced indentation of biological soft tissues". *BioMed research international,* **2017**.

[14] Mindlin, R., 1953. Force at a point in the interior of a semi-infinite solid. Tech. rep., Columbia University.

[15] Abramowitz, M., and Stegun, I. A., 1972. *Handbook of Mathematical Functions with Formulas, Graphs, and Mathematical Tables*. US Government Printing Office, Washington, D.C. 20402.

[16] Wagner, T. J. W., and Vella, D., 2013. "The 'Sticky Elastica': delamination blisters beyond small deformations". *Soft Matter,* **9**, pp. 1025–1030.

[17] Rice, J. R., 1968. "Mathematical analysis in the mechanics of fracture". In *Fracture: an advanced treatise*, H. Liebowitz, ed., Vol. 2. Academic Press, ch. 3, pp. 191–311.

[18] Tsai, V. C., and Rice, J. R., 2010. "A model for tur-

bulent hydraulic fracture and application to crack propagation at glacier beds". *Journal of Geophysical Research: Earth Surface,* ***115***(F3).

[19] Hewitt, D. R., Chini, G. P., and Neufeld, J. A., 2018. "The influence of a poroelastic till on rapid subglacial flooding and cavity formation". *Journal of Fluid Mechanics,* ***855***, pp. 1170–1207.

A   Basal Results

Here we present the corresponding results for the displacement that occurs at the base of the layer, where the pressure is applied. As expected, the basal and surface displacements are very similar in the $h \ll 1$ limit, and agree well with the bending-beam solutions discussed in §5. A comparison of the two-dimensional basal profiles from the extremes of our (h,K) parameter range is shown in Fig. 10. The various scalings for the two-dimensional basal displacement are listed in Tab. 6, and for the axisymmetric basal displacement in Tab. 7. The normalised basal profiles are qualitatively quite similar to the surface profiles shown in Fig. 2 for all but the $h \gg 1$, $K \gg 1$ case, which feels the strength of the foundation much more severely. Noticeably, outside of the pressure patch the basal displacement is minimal as the layer is held close to the foundation, but as $h \ll 1$ the point of zero displacement still occurs some distance away from the patch.

While the corresponding normalised profiles may be similar for a large portion of the parameter space, the characteristic features of the basal displacement are quantitatively quite different to those for the surface, however, as demonstrated by their differing scalings behaviours and the composite curves discussed in the Supplementary Material. Two key differences are that the maximum displacement at the base is insensitive to h for a thick layer, and that the maximum subsidence at the base is the only feature sensitive to K for a stiff foundation.

Table 6: Basal displacement scaling behaviours for two-dimensional deformations.

	$h \ll 1$	$h \gg 1$	$K \ll 1$	$K \gg 1$
$\max\{w_b\}$	h^{-3}	h^0	$K^{-3/4}$	K^0
$\min\{w_b\}$	$h^{-3/2}$	h^{-2}	$K^{-3/4}$	K^{-1}
x_b^0	h^0	h^1	$K^{-1/4}$	K^0

Table 7: Basal displacement scaling behaviours for axisymmetric deformations.

	$h \ll 1$	$h \gg 1$	$K \ll 1$	$K \gg 1$
$\max\{w_b\}$	h^{-3}	h^0	$K^{-1/2}$	K^0
$\min\{w_b\}$	$h^{-3/2}$	h^{-3}	$K^{-1/2}$	K^{-1}
x_b^0	h^0	h^1	$K^{-1/4}$	K^0

Fig. 10: Comparison of two-dimensional basal profiles for different (h,K) values. The solid blue curves are for the parameter values quoted while the dashed curves are the bending-beam solution (29) for $h = 10^{-4}$, $K = 10^8$. The dark-grey, obliquely hatched region shows the section of the displacement overlying the pressure patch, while the light-grey, vertically hatched region denotes the Winkler foundation.

List of Figures

List of Tables